Quantitative chemical mapping of InGaN quantum wells (QW) from calibrated high angle annular dark field (HAADF) micrographs.

Daniel Carvalho[1*], Francisco M. Morales[1], Teresa Ben[1], Rafael García[1], Andrés Redondo-Cubero[2,3], Eduardo Alves [2], Katharina Lorenz[2], Paul R. Edwards[4], Kevin P. O'Donnell[4], Christian Wetzel[5]

[1] *Departamento de Ciencia de los Materiales e I. M. y Q. I., Facultad de Ciencias, Universidad de Cádiz. Campus Río San Pedro 11510 Puerto Real, Cádiz*
[2] *1IPFN, Instituto Superior Técnico, Universidade de Lisboa, Estrada Nacional 10, km 139.7, 2695-066 Bobadela LRS, Portugal*
[3] *Departamento de Física Aplicada, Universidad Autónoma de Madrid, 28049 Madrid, Spain*
[4] *SUPA Department of Physics, University of Strathclyde, Glasgow, G4 0NG, Scotland,UK*
[5] *Department of Physics and Future Chips Constellation, Rensselaer Polytechnic Institute, Troy, New York 12180, USA*

Abstract.

We present a simple and robust method to acquire quantitative maps of compositional fluctuations in nanostructures from low magnification high angle annular dark field (HAADF) micrographs calibrated by energy dispersive X-ray (EDX) spectroscopy in scanning transmission electron microscopy (STEM) mode. We show that a non-uniform background in ~~the~~ HAADF-STEM micrographs can be eliminated, to a first approximation, by use of a suitable analytic function. The uncertainty in probe position when collecting an EDX spectrum renders the calibration of HAADF-STEM micrographs indirect, and a statistical approach has been developed to determine the position with confidence. Our analysis procedure, presented in a flowchart to facilitate the successful implementation of the method by users, was applied to discontinuous InGaN/GaN quantum wells in order to obtain quantitative determinations of compositional fluctuations on the nanoscale.

~~1.~~ Introduction

Due to its composition-tunable wide bandgap, which covers the visible and IR regions, and its high temperature stability, the semiconductor alloy InGaN is considered an essential material for

visible light sources. However, the manufacture of devices for an all-solid-state lighting system with this ternary alloy as the active component still faces a number of challenges. One of the bottlenecks is related to the efficiency droop, whose origin is still a topic of much debate (O'Donnell, et al., 2012); (Verzellesi, et al., 2013). Spectroscopic and microscopic investigations suggest that the high efficiency of InGaN based devices, despite their high dislocation density, depends upon local In/Ga atomic concentration fluctuations (Rosenauer, et al., 2011a); (Narayan, et al., 2002); (Lai, et al., 2006). These nanoscale centers act to localize charge carriers and prevent their diffusion to nonradiative traps such as dislocations. Hammersley, et al., (Hammersley, et al., 2011) and Watson-Parris, et al. (Watson-Parris, et al., 2010) have suggested that quantum well (QW) width variations play a similar role in localizing excitation. The tailoring of nanostructures to improve device operation has been a matter of discussion during the last decade and is still not well understood. These unsolved problems make InGaN an attractive topic for both the semiconductor technologist as well as the materials characterization community.

Among the available nanoscale characterization techniques, transmission electron microscopy (TEM) has been extensively and successfully used to characterize InGaN. (Gu, et al., 2009); (Özdöl, et al., 2010); (Kret, et al., 2010);(Rosenauer, et al., 2011b); (Rigutti, et al., 2013) In particular, scanning TEM (STEM), in high angle annular dark-field (HAADF) mode, offers chemical information through *Z-contrast*, with a strong dependence of the signal intensity on atomic number(Crewe, et al., 1970). This makes the interpretation of HAADF micrographs much more intuitive than in classical TEM. When electrons are scattered at high angles the scattering can be approximated as pure Rutherford scattering which allows quantitative elemental mapping of the spatial distribution of different elements by detection of the elastically scattered electrons (Pennycook, et al., 1986); (Walther, 2006).

Recently, a fewSome authors (Rosenauer, et al., 2011a); (Molina, et al., 2009); (Pantzas, et al., 2012) have reported the development of techniques to produce quantitative chemical maps of III-V semiconductor samples using *Z*-contrast imaging. In particular, Walther (Walther, 2006) and

Pantzas et al., (~~Pantzas, et al.,~~ 2012) obtained compositional maps from HAADF-STEM micrographs recorded at low magnifications; their methods proved to be extremely useful for analyzing large regions of interest. Pantzas et al., (~~Pantzas, et al.,~~ 2012) showed further that energy dispersive X-ray (EDX) spectroscopy could be used to transform qualitative *Z*-contrast maps into quantitative compositional maps: the combination uniquely exploits the chemical accuracy and spatial resolution of the two techniques.

In the present work we show that it is possible to characterize features in a STEM-HAADF micrograph on length scales similar to or even smaller than the STEM-EDX probe radius.~~,~~ ~~i~~It should be noted that for EDX measurements the focused electron beam had a radius of 1 nm while for HAADF imaging the focused beam had a radius of 0.5nm. ~~a~~A larger beam size was chosen to perform EDX in order increase the counts and thus the quality of the data acquired. We present a simple and robust procedure to obtain accurate quantification maps (after correcting the background contribution which arises due to the thickness inhomogeneity of the TEM specimen) by using a few points in the Z-contrast image calibrated by EDX compositional measurements. We successfully apply this method to map sample regions containing interrupted $In_xGa_{1-x}N$ QWs (with average x = 14%) to quantify their InN fraction on the nanoscale.

~~2. Experimental details~~Materials and Methods

The 5-period $In_xGa_{1-x}N$/GaN multi-quantum well (MQW) sample was grown on a GaN buffer layer on c-plane sapphire using metalorganic chemical vapo~~u~~r deposition (MOCVD). The growth conditions can be found elsewhere(Gerthsen, et al., 2000) The nominal QW thickness was 3 nm and the nominal superlattice period was 24 nm. Average InGaN compositions of the QWs were estimated by Rutherford Backscattering Spectrometry (RBS) and Wavelength Dispersive X-Ray (WDX) spectroscopy. RBS was performed with a 2 MeV beam, collimated to 0.2x0.6 mm^2 and a silicon surface barrier detector placed at 160º backscattering angle in Cornell geometry using grazing incidence geometries. RBS spectra were analyz~~s~~ed using the NDF code (Barradas & Jeynes, 2008). WDX was carried out using a 10 kV, 100 nA electron beam defocused to 20 µm

diameter in a Cameca SX100 electron probe micro-analyzer (EPMA) (O'Donnell, et al., 2004). The same equipment was used for cathodoluminescence measurements (CL) using a 5 kV, 100 pA, electron beam, defocused to an 8μm footprint.

Cross-sections of the samples were prepared for TEM inspection by classical methods of mechanical grinding and polishing. Electron transparency was then reached by Ar^{+}-milling using 3.5keV of ion voltage and ±5° of gun inclination with respect to the sample plane. Superficial amorphization was avoided in a final step by reducing the voltage and angle to 3keV and ±3°.

HAADF-STEM and EDX were performed on a JEOL 2010F microscope operating at 200kV, with a camera length of 80mm, HAADF detector angular range of 120mrad to 250mrad, emission current of 119µA and 9.5×10^{-10} A probe current. The EDX detector used was an Oxford X-Max^{N} 80 T model. All of the subsequent calculations were performed using Matlab®.

~~3.~~ RESULTS

Macroscopic compositional analysis

Figure 1a presents RBS spectra of the InGaN/GaN MQW for different incident angles, θ, of the analyzing beam. For close to normal incidence (θ =5°) the entire MQW region is revealed but individual QWs cannot be resolved. For higher inclination angles it is possible to resolve the near-surface QWs, the In signal from deeper wells being obscured by an overlap with the Ga signal at high angles. However, due to the limited depth resolution it is not possible to determine unambiguously both the thickness and composition of the QWs from RBS alone. Therefore the QW thickness was fixed at the nominal value of ~3 nm (confirmed by TEM as seen below) and a simultaneous fit to all spectra (see Figure 1) yielded an average InN molar fraction of ~~(~~14.6±0.5~~)~~%. The RBS spectra furthermore showed that the composition of all 5 QWs is similar and the nominal MQW period of ~24 nm was also confirmed. The average QW composition was further confirmed by WDX measurements yielding ~~(~~14.2±0.6~~)~~% InN content. For the WDX analysis a mean InN fraction was measured assuming a uniform composition throughout the probed depth. The latter was

determined with the help of Monte Carlo simulations. ~~The a~~Average composition of the QWs was then determined assuming the nominal QW thickness and period. Figure 1b shows the room temperature CL spectrum: the MQW structure was found to emit around 573nm.

~~4.~~ Microscopy~~ic~~ analysis~~: methodology~~

For HAADF-STEM when almost all the electrons reaching the detector are elastically scattered the intensity of a micrograph can be approximated by:

$$I^{micrograph} \propto \zeta(t) \cdot Z^{\varepsilon} \qquad \textit{Eq (1)}$$

Where $\zeta(t)$ is a function that depends on the thickness t of the TEM specimen, Z is the atomic number and the exponent ε a constant which lies in the range $1.7 < \varepsilon < 2$ (Jesson & Pennycook, 1995). Consulting previous reports the minimum inner angle of the detector should be greater than 80mrad if a pure Rutherford scattering that predicts $\varepsilon = 2$ can be assumed.(Liu, et al., 2008; Pennycook, et al., 2000) Since in this work the inner angle was 120mrad we can set $\varepsilon = 2$ in agreement with recent proposals (Pantzas, et al., 2012; Walther, 2006).

To account for the image background, the thickness dependent term (Van den Broek, et al., 2012) is considered as:

$$\zeta(t) = I_0(1 - e^{-Qt}) \qquad \textit{Eq (2)}$$

Where Q is the total elastic scattering cross section and I_0 is the incoming beam intensity. This equation can be expanded as:

$$\zeta(t) = I_0 Qt - \frac{I_0}{2}(Qt)^2 \qquad \textit{Eq (3)}$$

The second term of Eq. (3) cannot be neglected for large specimen thicknesses. Since the aim of the present work is to map relatively large regions, the intensity in a HAADF-STEM image should not

only be scaled by the effective atomic number[1] Z_{eff} of all species involved in the analyzsed region, but also by $\zeta(t)$. Thus, the micrograph signal has to be approximated as:

$$I^{micrograph} \propto {Z_{eff}}^2 \cdot \zeta(t) \qquad \textit{Eq (4)}$$

To minimize the effect of thickness variations on the micrograph intensity, a background correction function should be applied with the form of Eq. (4), i.e.:

$${Z_{eff(Ref)}}^2 \cdot \zeta(t) \qquad \textit{Eq (5)}$$

To demonstrate our approach to the case of InGaN QWs, Figure 2a shows a raw HAADF-STEM image of the sample to be studied. The background function above is approximated by masking the features of interest (the QWs) and any other artefacts in the image other than the reference GaN barriers as shown in Figure 2b, thus avoiding their contribution to the fitting. The unmasked region is then fitted to a polynomial (in this case a 5th order polynomial in *x* and *y*).

In order to produce a normalized image, the intensity of the original micrograph is divided through by this background function and its interpolation to the masked regions $({Z_{eff(GaN)}}^2 \zeta(t)_{GaN})$; (Figure 2c). The normalized intensity distribution is thus:

$$I^{normaliszed} \propto \frac{{Z_{eff(InGaN)}}^2 \cdot \zeta(t)_{InGaN}}{{Z_{eff(GaN)}}^2 \cdot \zeta(t)_{GaN}} \qquad \textit{Eq (6)}$$

We therefore obtain, using Eq. (3), the (normalized) map in terms of scattering cross section, *Q*:

$$I^{normaliszed} \propto \frac{{Z_{eff(InGaN)}}^2 \cdot (Q_{InGaN} - \frac{1}{2} t \cdot {Q_{InGaN}}^2)}{{Z_{eff(GaN)}}^2 \cdot (Q_{GaN} - \frac{1}{2} t \cdot {Q_{GaN}}^2)} \qquad \textit{Eq (7)}$$

Next, to check the dependence of the normalized intensity on the variation of InN concentration in InGaN, the total cross section for elastic scattering Q is calculated using routines from Egerton (Egerton, 2011). For $In_xGa_{(1-x)}N$ the square root of the normalized intensity *versus*

[1] Where: $Z_{eff} \approx \frac{\sum_i f_i Z_i^{1.3}}{\sum_i f_i Z_i^{0.3}}$ and f_i is the atomic fraction of each element of atomic number Z_i . Egerton, R.F. (2011). *Electron Energy-Loss Spectroscopy in the Electron Microscope*. NY, USA: Springer.).

the InN content (x) and layer thickness t, from 0 to 200 nm, is shown in Figure 3. Note that $\sqrt{I^{normalised}}$ is directly proportional to x for cases where the InN concentration (the contour plot in Figure 3 shows the residual, in percentage $(\frac{\Delta\sqrt{I^{normalised}}}{\sqrt{I^{normalised}}} \times 100)$, of the linear fit to the normalized intensity). Since the nominal composition of our studied QW is $In_{0.14}Ga_{0.86}N$ this approximation makes calibrating the HAADF micrographs straightforward as we can relate the intensity to the composition directly.

5. Microscopy~~ic analysis:~~ quantification

In InGaN the 58% difference between the atomic numbers of Ga (31) and In (49) allows an *a priori* assumption that InN-rich regions will tend to be brighter than GaN-rich ones.

Taking into account the approximations mentioned above the next step is to divide the HAADF-STEM image into a number of sub-regions (SR) ensuring that each SR is imaged under the same experimental conditions. In every SR, local calibration points (LCPs) are defined. The composition of these points is known (e.g., by EDX measurements) and they are specifically chosen such that the maximum or minimum intensity in the SR are registered. In particular each SR is defined by 3 non-collinear points, and for computational ease the LCPs define these points.

Once an LCP is defined, the volume of interaction of the electron beam in the sample must be calculated. For this work Monte-Carlo simulations using Casino® (Verzellesi, et al., 2013) were used (process not shown). The interaction volume for our imaging conditions was found to approach a cylinder with a radius of ~1nm. Using this information the value extracted from a point EDX spectrum can be associated to an intensity for each LCP of a given SR. With this aim the volume under the surface of the interaction region can be calculated in the following way.

$$Volume = \int_k^n \int_l^m I \cdot ds = \sum_{k,l}^{n,m} I_{ij}.s_{ij} \qquad \textit{Eq (8)}$$

The total surface S_{tot} of this interaction volume is:

$$S_{tot} = \sum_{k,l}^{n,m} s_{ij} \qquad \textit{Eq (9)}$$

Where I_{ij} is the intensity and s_{ij} is the area of the i^{th} element of the j^{th} column of the matrix which encompasses the region on the sample where the EDX was taken. The total volume is consequently:

$$Volume = I_{average} \cdot S_{tot} \qquad \textit{Eq (10)}$$

Using Equation (9) in (11) the HAADF-STEM intensity corresponding to the composition acquired by EDX at that point can be rewritten as:

$$I_{average} = \frac{\sum_{i,j}^{n,m} I_{ij} . s_{ij}}{S_{tot}} \qquad \textit{Eq (11)}$$

The $I_{average}$ is calculated for all three LCP of a given SR. This gives us the maximum intensity for the LCP where the maximum InN content was detected by EDX, ($I_{max} = I_{average}$ where EDX gave a maximum InN concentration) and minimum intensity ($I_{min} = I_{average}$ where EDX gave a minimum InN concentration) for every SR. Now that the upper and lower bounds of the intensity and composition for each SR have been acquired, the composition for intermediate intensities is obtained by linear interpolation, using a calibration constant K for the SR:

$$K = \frac{\mathrm{I}_{max} - \mathrm{I}_{min}}{comp_{max} - comp_{min}} \qquad \textit{Eq (12)}$$

Here, $comp_{max}$ and $comp_{min}$ are compositions produced by EDX of the maximum and minimum points of the SR. The full SR can then be calibrated with the following equation:

$$comp_{SR} = comp_{max} - \frac{\mathrm{I}_{max} - \mathrm{I}_{SR}}{K} \qquad \textit{Eq (13)}$$

During acquisition of the point EDX spectra it was noticed that the probe beam had a tendency to move when the spectrum was taken in positions near the InGaN/GaN interfaces. This could be due to small beam drifts or charging of the specimen which are common in electron microscopy (Kim, et al., 2010). When a finely focused probe is incident on the specimen the incident electrons excite the internal electrons of the specimen. This excitation causes the electrons

from the valance band to reach various permitted states above the Fermi level. In semiconductors, unless these excited electrons are produced close to the surface, they are internal secondary electrons that travel through the specimen and produce further frenkel pairs. Due to the low electron concentration of electrons in the conduction band the vacancies left behind by the un-bounded electrons are not neutralized and therefore in order to reach electrostatic equilibrium electrons from the surrounding (mainly the grounded grid) flow towards the uncompensated region this process takes place on a time scale of a few femtoseconds. Due to the limited conductance of the sample the compensating electrons almost never fully compensate the positive charges left behind in the illuminated region. Thus creating an electric potential and an induced electric field. According to theoretical calculations by Cazaux et al.(~~Cazaux,~~ 1995) the field can be in the order of 10^{10} V/m. Using the simple approximation of an electron beam in an electric field, for a 100nm thick specimen and 10^{10} V/m field, the incident electron beam will experience a deflection of about 0.5 Å. The calculations did not consider an inhomogeneous structure, as is the case here. When the structures of interest present fluctuations on a sub-probe length scale the cylindrical charged column argument does not hold. Although the probe illuminated region can be treated as a nano-column the field components change~~s~~ drastically due to the inhomogeneous dielectric distribution within or near the nano column. ~~In this case f~~For these examples not only will the quantum wells ~~e~~affect the electric field ~~but also~~and the compositional fluctuations within the well will have a significant effect on the field and can enhance it. An example of the effect can be seen in Figure 4a where the stain, generated due to carbon contamination on the TEM specimen, indicating the interaction region, which is about the size of the electron beam footprint as seen from the profile in Figure 4b, is slightly displaced from the intended region (center of the QW). Although this deflection caused the calibration to be made within a couple of nanometers of the intended position, the features of interest are themselves of a similar length scale and ~~it~~ cannot be ignored. The deflection causes the SRs to be calibrated with different constants K due to the uncertainty in this position, leading to fragmentation of features in the composition map. An example of this can be seen for the first QW,

shown in Figure 5 a,b, where a prominent apparent discontinuity in the well composition appears (Figures 5c and d) due to displaced calibration data.

To overcome the effects of such uncertainty in the probe position we propose a statistical refinement of the technique ~~which~~ that involves (1) iteratively changing the center of the LCP corresponding to the intensity maximum (we scan the LCP with the intensity maximum since it represents the InN richer region) and (2) recalculating the calibration constant *K* at every new position. In this way the entire region within the uncertainty of the probe position is scanned. Figure 6a illustrates the acquisition procedure. The set of calibration constants is stored in an array; this is done for all the SRs in a micrograph. Once a collection of all the probable *K* values of the SRs is obtained they are represented in a histogram. The limits of the *K* values that would be included in the distribution fit are then chosen. Figure 6b shows the histogram along with the values included, highlighted in pink, the selected data is then fitted to a Gaussian curve and the expected value of the fit is then set as the most probable calibration constant. Once the most probable calibration constant has been statistically determined, the LCP is set to that position in the SR that yields a calibration constant closest to the most probable value. This new constant is then used to recalibrate the SR and acquire a refined composition map as shown in Figure 6c where the discontinuities apparent in Figure 5 have been eliminated.

To summarize the above described procedure, the steps that should be followed to compute compositional maps are reviewed in the flow chart of Figure 7.

~~6.~~ Application to interrupted InGaN QWs

The method described in Section 5 was applied to a HAADF-STEM image of an InGaN MQW sample. Figure 8a shows a low magnification HAADF-STEM micrograph and Figure 8b the associated temperature-scale intensity map of the sample. Some typical threading dislocations (TD) and V-type defects were observed. Figure 8c features interruptions in the QWs (marked with yellow inverted triangles) and brightness variations within the same well. In Figure 8d a higher

magnification temperature-scale image is shown with the contrast adjusted in order to emphasize intensity changes within a single QW, which can be attributed to compositional variations. Such variations, not uncommon (Kisielowski, et al., 1997), can be explained by a large difference in the free binding enthalpies of InN and GaN (Mayrock, et al., 2000). The inset in Figure 8d shows the original image.

The background is accounted for as commented earlier by masking the InGaN QWs and artefacts, next fitting the background to a 5th order polynomial, and later dividing the original image intensity by the calculated background ~~one~~ and taking its square root. Because of the discontinuous nature of the wells, there will be a contribution of the surrounding GaN layer to the composition measured by EDX. To overcome this problem, every QW was analyzed independently. Each QW was divided into a number of SR with LCPs at their respective vertices. Figure 9 (a-e) show the meshed SRs of QWs 1 to 5 respectively and the corresponding EDX-measured compositions of the LCPs are presented in Table 1. For this case the region of uncertainty was set to no more than 1 nm.

In individual uncorrected compositional maps acquired for all five QWs, Figure 10(a-e), QWs appear to have very different average InN content, contrary to what was observed by RBS. The change in thicknesses, discussed above, seriously compromises the EDX measurements ~~this is~~ due to ~~the~~ contributions the surrounding GaN layer has on the EDX signal in the case of interrupted QWs. It is therefore necessary to recalibrate the composition of the QWs with respect to the average InN content determined by RBS and WDX. The background noise is first measured by drawing a line profile just below the QW (Figure 11a). An example of the extracted background noise can be observed in Figure 11b. The intensity values in the background line profile are then plotted in a histogram, Figure 11c. Pixels with a higher value than the limit (marked with a blue line for this QW) are used to calculate an average (apparent) InN content in the well ($InN_{average}$). The corrected composition is then simply:

$$correctedmap = \frac{uncorrectedmap}{InN_{average}} \times mean_{InN} \quad \text{Eq (14)}$$

Where the $mean_{InN}$ is the composition acquired from RBS and WDX measurements. Figure 12 shows this final composition map obtained by reconstructing the micrograph with the corrected composition values. The InN fluctuations within each well are striking, even though the image was obtained at relatively low magnification. The maximum InN content within any QW is significantly (>50%) higher than the average InN content estimated by WDX and RBS. The InN content corresponding to the peak CL emission wavelength (Hsu, et al., 2014) is closer to 30%. The InN content in the InN-rich regions, measured by the method presented here (≈ 25%) agrees well with that calculated from the emission peak. The main difference in macroscopic measurements such as RBS and WDX as compared to microscopy~~ic~~ techniques such as EDX-STEM is that RBS and WDX can detect the average InN content of the wells, but are not able to determine the local composition on a nm scale. STEM-EDX on the other hand is capable of detecting these fluctuations, but is limited by the projection problem making it difficult to quantify the InN content. Only a correlation of these techniques with HAADF-STEM could detect the presence of high InN clusters thus explaining the emission peak.

7. Conclusions

Interrupted InGaN/GaN QWs were characterized by TEM, RBS, WDX, and CL. The synergy of these techniques allows a complete compositional analysis of the structure while the composition of the wells could not be unambiguously determined by any one characterization technique independently. We presented a relatively straightforward technique to calibrate HAADF-STEM micrographs using a minimum number of LCPs extracted by EDX measurements. Compositional fluctuations within the well could be distinguished using low magnification micrographs. The fluctuations in the HAADF-STEM micrograph background signal and the deviation of the rooted normalized intensity form a plane, as shown in figure 11b and figure 3

respectively, are insignificant compared to the uncertainty of the composition value acquired by EDX (as high as 1% in some cases). We can thus attribute the error of this method to the error of the EDX measurement. Due to the confined nature of the QWs, the EDX-HAADF-STEM acquired compositions were less than the average value determined by RBS/WDX. Recalibration of the EDX-HAADF-STEM data by this average composition reconciled the different techniques. Fluctuations on a length scale smaller than the EDX probe size were successfully mapped and analyzed quantitatively. Regions of high InN content (x≈25%) were observed and can account for the bright yellow light emission of a structure with an average InN content about half of that. The developed technique can be extended to other ternary alloys and 3D confined structures.

Acknowledgements

This work was supported by the MAT2010-15206 (CICYT, Spain), EU-COST Action MP0805, and P09-TEP-5403 (Junta de Andalucía with EU-FEDER participation). We acknowledge support by FCT Portugal (PTDC/FIS-NAN/0973/2012, SFRH/BPD/74095/2010, Investigador FCT), and Juan de la Cierva program (JCI-2012-14509). D.C. thanks D. F. Reyes for the discussions during the preparation of the manuscript. The authors thank the anonymous reviewers for extremely useful suggestions and pointing out inaccuracies in the original manuscript.

Figure captions

Figure. 1. a) RBS spectra of the InGaN/GaN MQW taken with different incident angles of the analyzing beam. All spectra were simultaneously fitted using the NDF code (red lines). b) Shows a room temperature CL spectrum.

Figure 2. a) Raw HAADF-STEM micrograph of the QWs sample, b) Micrograph where the mask ~~has been~~was applied in specific regions (the contrast was changed before fitting) and c) final background corrected image.

Figure 3) Plot of $\sqrt{\frac{Z_{eff(InGaN)}{}^2\cdot(Q_{InGaN}-\frac{1}{2}tQ_{InGaN}{}^2)}{Z_{eff(GaN)}{}^2\cdot(Q_{GaN}-\frac{1}{2}tQ_{GaN}{}^2)}}$ versus x in an $In_xGa_{(1-x)}N$ alloy and specimen thickness t from 0 to 200nm and the linear fit. The contour shows the residue to the linear fit.

Figure 4. a) HAADF-STEM image showing a region damaged by the electron beam after the acquisition of a spectrum indicating an example of the position of the probe, b) line profile extracted from this area in the image which shows that the damaged region has a diameter of about 2 nm.

Figure 5. a) The raw image of the first QW where a compositional map was acquired in InGaN sample, b) Magnified region of the QW marked in (a). c) and d) show the composition map acquired for the first QW in InGaN sample corresponding to images a and b, respectively. In b) and d) the discontinuous region of the QW is magnified to appreciate the difference in the calibration conditions.

Figure 6. a) Representation in a HAADF-STEM image of the spot refinement process, the first red circle in the left image designates the point where the EDX spectrum is recorded, and the other circles in the right image represent the virtual probe which is scanned over the region of uncertainty, b) Histogram of *K*-values measured in all ~~of~~ SRs. The values for calculating most probable *K*-value were chosen from the region with more counts (pink region) c) Final compositional color map of the QW along with the region magnified where the discontinuity as seen in Figure 5 is quenched.

Figure 7. Shows a flow chart that summarized the procedure presented in this work.

Figure8. a-b) Low magnification HAADF-STEM micrograph of the QW sample and its temperature scale. c) Micrograph showing the discontinuities in the wells (marked with inverted yellow triangles). d) High magnification Z-contrast image of a QW in color scale where InN fluctuations can be noticed, the inset shows the original image in grey scale.

Figure 9. (a-e) HAADF-STEM images showing the meshed SRs of the QWs 1 to 5 respectively with their LCPs.

Figure 10. a-e) shows the composition maps of the QWs 1-5 respectively, before normalization.

Figure 11. Composition map of the QW, the white line indicates~~d~~ the position from where the noise was measured. b) Shows the line profile c) the histogram of the background fluctuations.

Figure 12. Temperature scale image color compositional map finally obtained for the InGaN region analyzed.

Table 1. EDX composition values measured at the LCPs of the corresponding QWs displayed in Figure 10.

BARRADAS, N.P. & JEYNES, C. (2008). Advanced physics and algorithms in the IBA DataFurnace. Nuclear Instruments and Methods in Physics Research Section B: Beam Interactions with Materials and Atoms **266**(8), 1875-1879.

CAZAUX, J. (1995). Correlations between ionization radiation damage and charging effects in transmission electron microscopy. Ultramicroscopy **60**(3), 411-425.

CREWE, A.V., WALL, J. & LANGMORE, J. (1970). Visibility of Single Atoms. Science **168**(3937), 1338-1340.

EGERTON, R.F. (2011). *Electron Energy-Loss Spectroscopy in the Electron Microscope*. NY, USA: Springer.

GERTHSEN, D., HAHN, E., NEUBAUER, B., ROSENAUER, A., SCHÖN, O., HEUKEN, M. & RIZZI, A. (2000). Composition Fluctuations in InGaN Analyzed by Transmission Electron Microscopy. physica status solidi (a) **177**(1), 145-155.

GU, G.H., PARK, C.G. & NAM, K.B. (2009). Inhomogeneity of a highly efficient InGaN based blue LED studied by three-dimensional atom probe tomography. physica status solidi (RRL) – Rapid Research Letters **3**(4), 100-102.

HAMMERSLEY, S., BADCOCK, T.J., WATSON-PARRIS, D., GODFREY, M.J., DAWSON, P., KAPPERS, M.J. & HUMPHREYS, C.J. (2011). Study of efficiency droop and carrier localisation in an InGaN/GaN quantum well structure. physica status solidi (c) **8**(7-8), 2194-2196.

HSU, Y.-C., LO, I., SHIH, C.-H., PANG, W.-Y., HU, C.-H., WANG, Y.-C., TSAI, C.-D., CHOU, M.M.C. & HSU, G.Z.L. (2014). Green light emission by InGaN/GaN multiple-quantum-well microdisks. Applied Physics Letters **104**(10), -.

JESSON, D.E. & PENNYCOOK, S.J. (1995). Incoherent Imaging of Crystals Using Thermally Scattered Electrons. Proceedings of the Royal Society of London. Series A: Mathematical and Physical Sciences **449**(1936), 273-293.

KIM, Y.-M., JEONG, H., HONG, S.-H., CHUNG, S.-Y., LEE, J. & KIM, Y.-J. (2010). Practical Approaches to Mitigation of Specimen Charging in High-Resolution Transmission Electron Microscopy. Journal of Analytical Science & Technology **1**(2), 134-140.

KISIELOWSKI, C., LILIENTAL-WEBER, Z. & NAKAMURA, S. (1997). Atomic Scale Indium Distribution in a GaN/$In_{0.43}Ga_{0.57}N$/$Al_{0.1}Ga_{0.9}N$ Quantum Well Structure. Japanese Journal of Applied Physics **36**, 6932.

KRET, S., IVALDI, F., SOBCZAK, K., CZERNECKI, R. & LESZCZYŃSKI, M. (2010). Inhomogeneities of InGaN/GaN MOVPE multi quantum wells grown with a two temperatures process studied by transmission electron microscopy. physica status solidi (a) **207**(5), 1101-1104.

LAI, Y.-L., LIU, C.-P. & CHEN, Z.-Q. (2006). Tuning the emitting wavelength of InGaN/GaN superlattices from blue, green to yellow by controlling the size of InGaN quasi-quantum dot. Thin Solid Films **498**(1–2), 128-132.

LIU, F., COLLAZO, R., MITA, S., SITAR, Z., PENNYCOOK, S.J. & DUSCHER, G. (2008). Direct Observation of Inversion Domain Boundaries of GaN on c-Sapphire at Sub-ångstrom Resolution. Advanced Materials **20**(11), 2162-2165.

MAYROCK, O., WÜNSCHE, H.J. & HENNEBERGER, F. (2000). Polarization charge screening and indium surface segregation in (In,Ga)N/GaN single and multiple quantum wells. Physical Review B **62**(24), 16870-16880.

MOLINA, S.I., SALES, D.L., GALINDO, P.L., FUSTER, D., GONZÁLEZ, Y., ALÉN, B., GONZÁLEZ, L., VARELA, M. & PENNYCOOK, S.J. (2009). Column-by-column compositional mapping by Z-contrast imaging. Ultramicroscopy **109**(2), 172-176.

NARAYAN, J., WANG, H., YE, J., HON, S.-J., FOX, K., CHEN, J.C., CHOI, H.K. & FAN, J.C.C. (2002). Effect of thickness variation in high-efficiency InGaN/GaN light-emitting diodes. Applied Physics Letters **81**(5), 841-843.

O'DONNELL, K.P., AUF DER MAUR, M., DI CARLO, A., LORENZ, K. & THE, S.C. (2012). It's not easy being green: Strategies for all-nitrides, all-colour solid state lighting. physica status solidi (RRL) – Rapid Research Letters **6**(2), 49-52.

O'DONNELL, K.P., FERNANDEZ-TORRENTE, I., EDWARDS, P.R. & MARTIN, R.W. (2004). The composition dependence of the InxGa1−xN bandgap. Journal of Crystal Growth **269**(1), 100-105.

ÖZDÖL, V.B., KOCH, C.T. & VAN AKEN, P.A. (2010). A nondamaging electron microscopy approach to map In distribution in InGaN light-emitting diodes. Journal of Applied Physics **108**(5), -.

PANTZAS, K., PATRIARCHE, G., TROADEC, D., GAUTIER, S., MOUDAKIR, T., SURESH, S., LARGEAU, L., MAUGUIN, O., VOSS, P.L. & OUGAZZADEN, A. (2012). Nanometer-scale, quantitative composition mappings of InGaN layers from a combination of scanning transmission electron microscopy and energy dispersive x-ray spectroscopy. Nanotechnology **23**(45), 455707.

PENNYCOOK, S.J., BERGER, S.D. & CULBERTSON, R.J. (1986). Elemental mapping with elastically scattered electrons. Journal of Microscopy **144**(3), 229-249.

PENNYCOOK, S.J., RAFFERTY, B. & NELLIST, P.D. (2000). Z-contrast Imaging in an Aberration-corrected Scanning Transmission Electron Microscope. Microscopy and Microanalysis **6**(04), 343-352.

RIGUTTI, L., BLUM, I., SHINDE, D., HERNÁNDEZ-MALDONADO, D., LEFEBVRE, W., HOUARD, J., VURPILLOT, F., VELLA, A., TCHERNYCHEVA, M., DURAND, C., EYMERY, J. & DECONIHOUT, B. (2013). Correlation of Microphotoluminescence Spectroscopy, Scanning Transmission Electron Microscopy, and Atom Probe Tomography on a Single Nano-object Containing an InGaN/GaN Multiquantum Well System. Nano Letters **14**(1), 107-114.

ROSENAUER, A., MEHRTENS, T., MÜLLER, K., GRIES, K., SCHOWALTER, M., VENKATA SATYAM, P., BLEY, S., TESSAREK, C., HOMMEL, D., SEBALD, K., SEYFRIED, M., GUTOWSKI, J., AVRAMESCU, A., ENGL, K. & LUTGEN, S. (2011a). Composition mapping in InGaN by scanning transmission electron microscopy. Ultramicroscopy **111**(8), 1316-1327.

ROSENAUER, A., THORSTEN, M., MÜLLER, K., GRIES, K., SCHOWALTER, M., STEPHANIE, B., PARLAPALLI VENKATA, S., AVRAMESCU, A., KARL, E. & STEPHAN, L. (2011b). 2D-composition mapping in InGaN without electron beam induced clustering of indium by STEM HAADF Z-contrast imaging. Journal of Physics: Conference Series **326**(1), 012040.

VAN DEN BROEK, W., ROSENAUER, A., GORIS, B., MARTINEZ, G.T., BALS, S., VAN AERT, S. & VAN DYCK, D. (2012). Correction of non-linear thickness effects in HAADF STEM electron tomography. Ultramicroscopy **116**(0), 8-12.

VERZELLESI, G., SAGUATTI, D., MENEGHINI, M., BERTAZZI, F., GOANO, M., MENEGHESSO, G. & ZANONI, E. (2013). Efficiency droop in InGaN/GaN blue light-emitting diodes: Physical mechanisms and remedies. Journal of Applied Physics **114**(7), -.

WALTHER, T. (2006). A new experimental procedure to quantify annular dark field images in scanning transmission electron microscopy. Journal of Microscopy **221**(2), 137-144.

WATSON-PARRIS, D., GODFREY, M.J., OLIVER, R.A., DAWSON, P., GALTREY, M.J., KAPPERS, M.J. & HUMPHREYS, C.J. (2010). Energy landscape and carrier wave-functions in InGaN/GaN quantum wells. physica status solidi (c) **7**(7-8), 2255-2258.

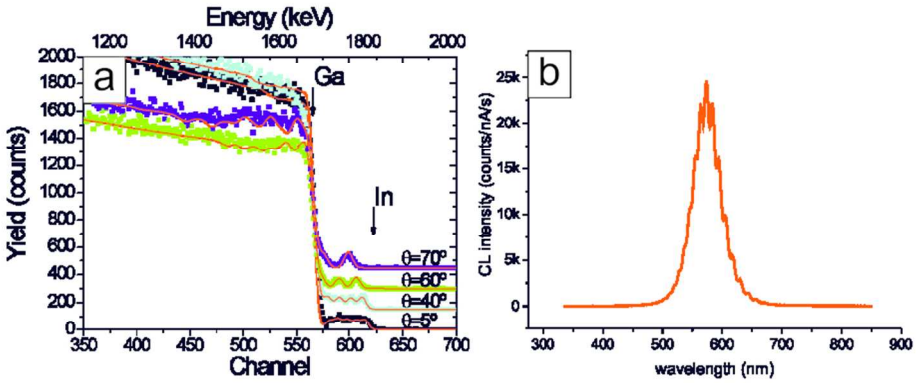

a) RBS spectra of the InGaN/GaN MQW taken with different incident angles of the analyzing beam. All spectra were simultaneously fitted using the NDF code (red lines). b) Shows a room temperature CL spectrum.
85x36mm (300 x 300 DPI)

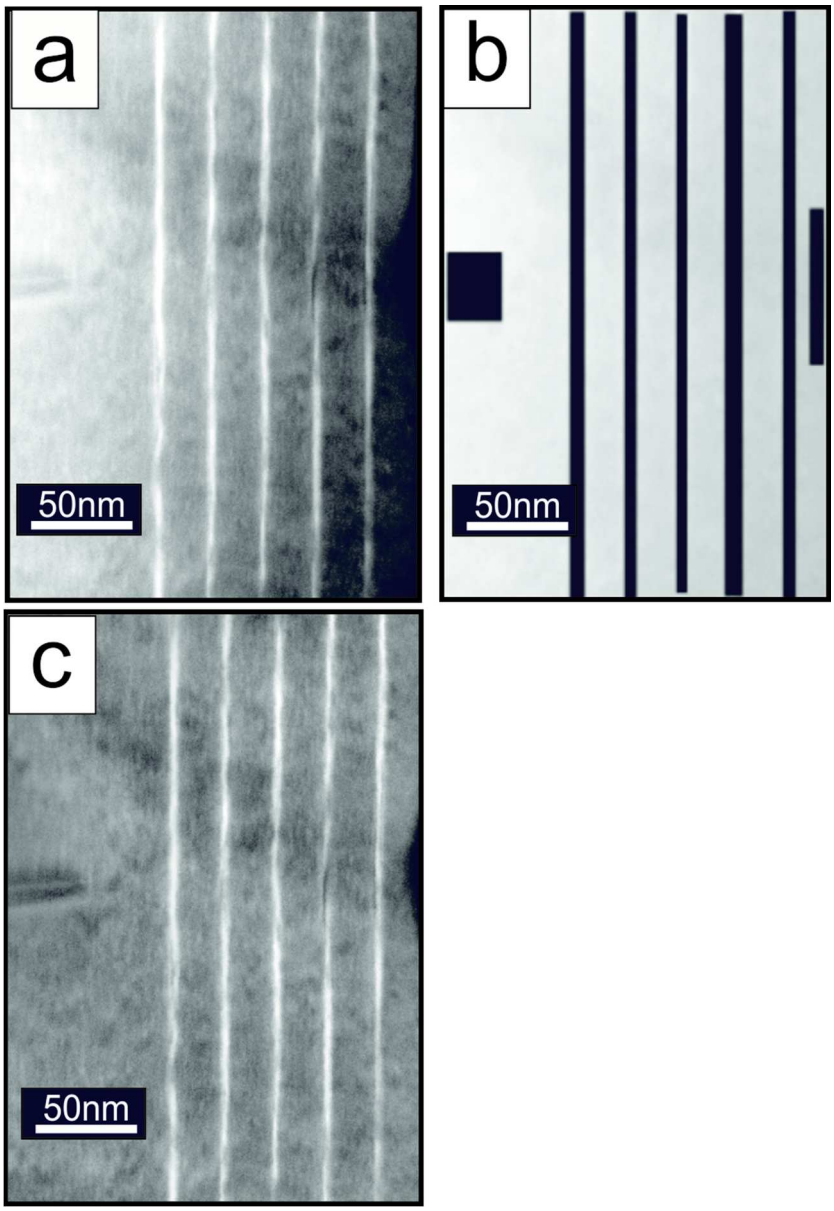

a) Raw HAADF-STEM micrograph of the QWs sample, b) Micrograph where the mask has been applied in specific regions (the contrast was changed before fitting) and c) final background corrected image.
85x123mm (300 x 300 DPI)

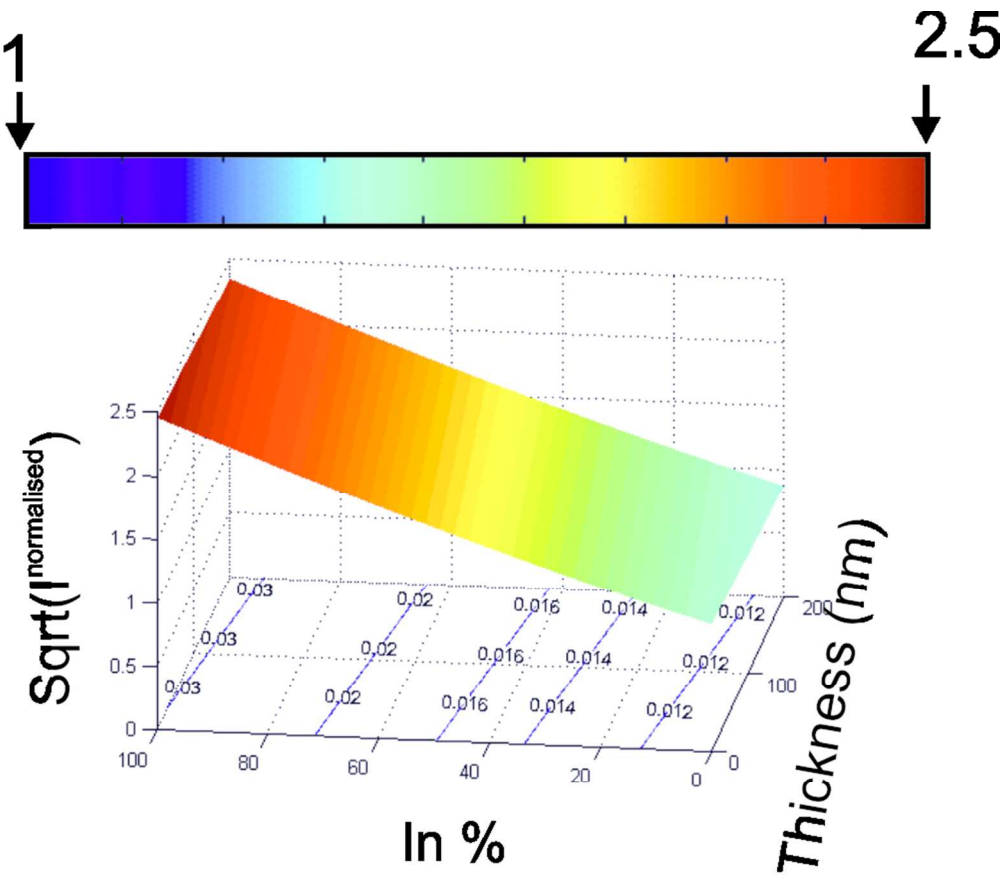

Figure 3) Plot of √((〖Z_eff(InGaN)〗^2·(Q_InGaN-1/2 〖〖tQ〗_InGaN〗^2))/(〖Z_eff(GaN)〗^2·(Q_GaN-1/2 t〖Q_GaN〗^2))) versus x in an 〖In〗_x 〖Ga〗_((1-x)) N alloy and specimen thickness t from 0 to 200nm and the linear fit. The contour shows the residue to the linear fit.
85x73mm (300 x 300 DPI)

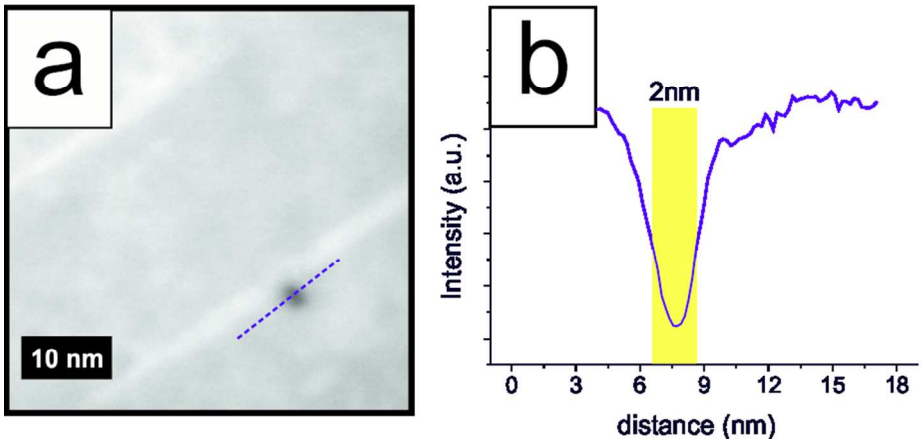

a) HAADF-STEM image showing a region damaged by the electron beam after the acquisition of a spectrum indicating an example of the position of the probe, b) line profile extracted from this area in the image which shows that the damaged region has a diameter of about 2 nm.
85x37mm (300 x 300 DPI)

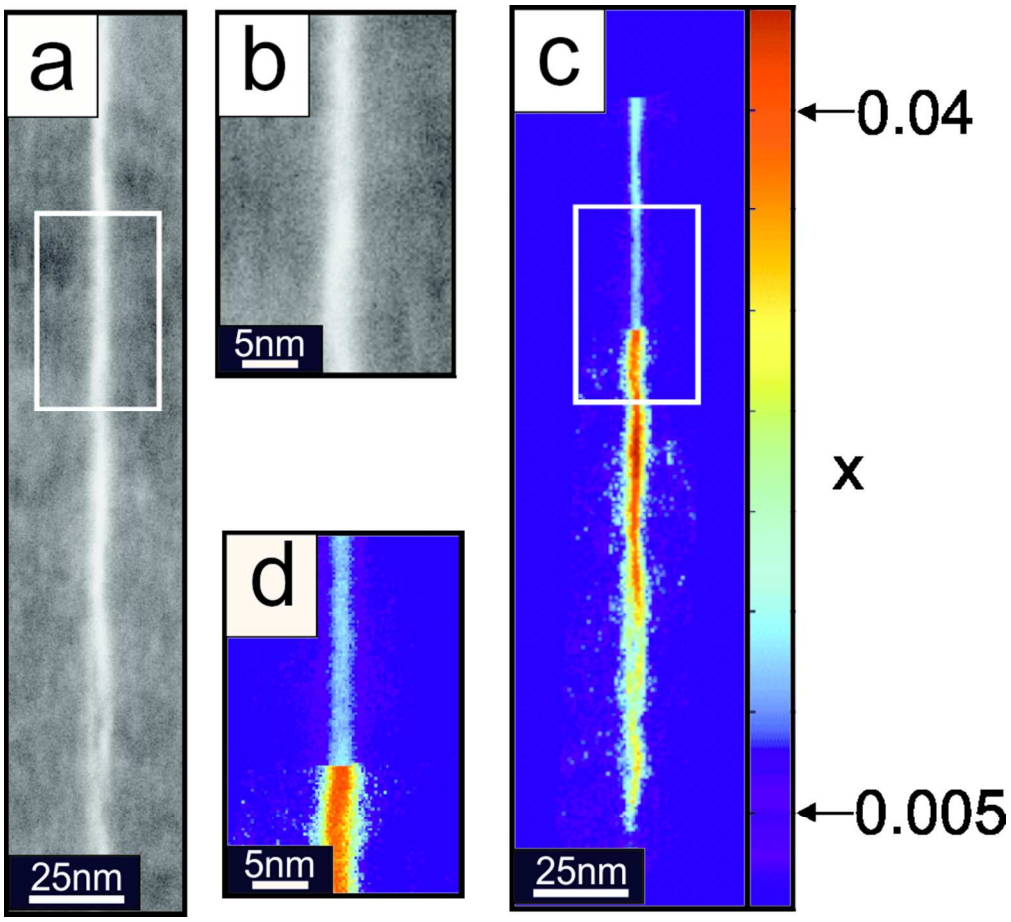

. a) The raw image of the first QW where a compositional map was acquired in InGaN sample, b) Magnified region of the QW marked in (a). c) and d) show the composition map acquired for the first QW in InGaN sample corresponding to images a and b, respectively. In b) and d) the discontinuous region of the QW is magnified to appreciate the difference in the calibration conditions.
85x77mm (300 x 300 DPI)

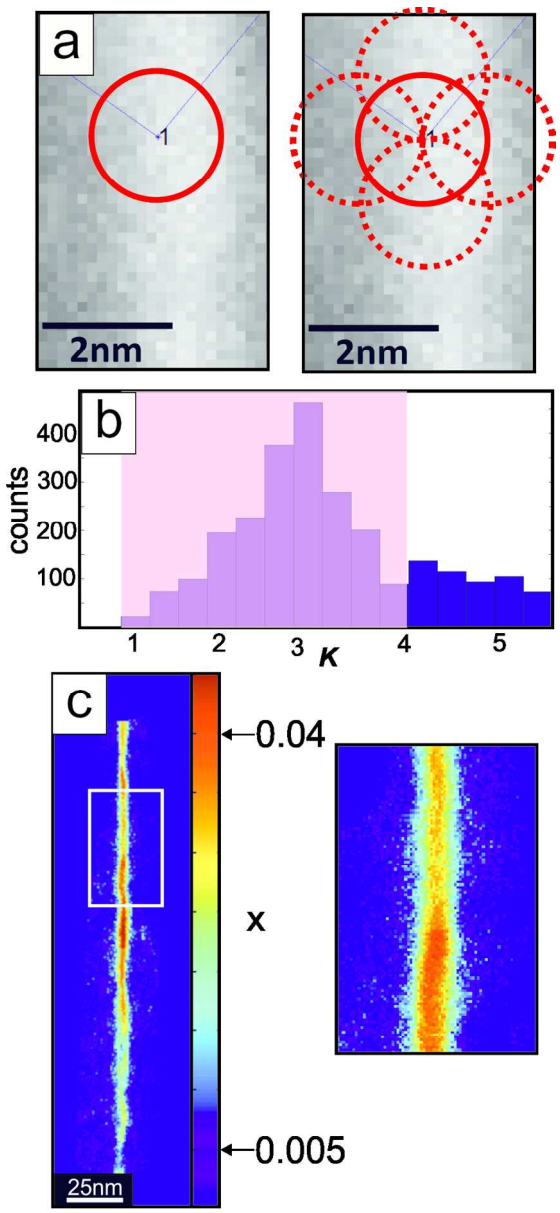

. a) Representation in a HAADF-STEM image of the spot refinement process, the first red circle in the left image designates the point where the EDX spectrum is recorded, and the other circles in the right image represent the virtual probe which is scanned over the region of uncertainty, b) Histogram of K-values measured in all of SRs. The values for calculating most probable K-value were chosen from the region with more counts (pink region) c) Final compositional color map of the QW along with the region magnified where the discontinuity as seen in Figure 5 is quenched.
85x185mm (300 x 300 DPI)

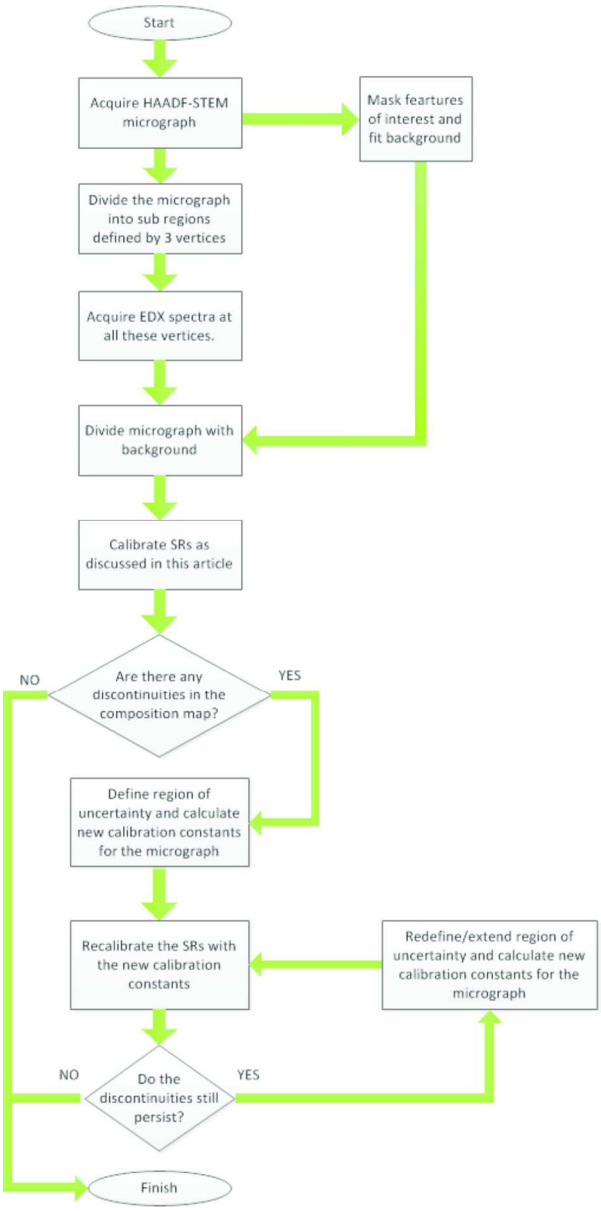

Shows a flow chart that summarized the procedure presented in this work.
85x171mm (300 x 300 DPI)

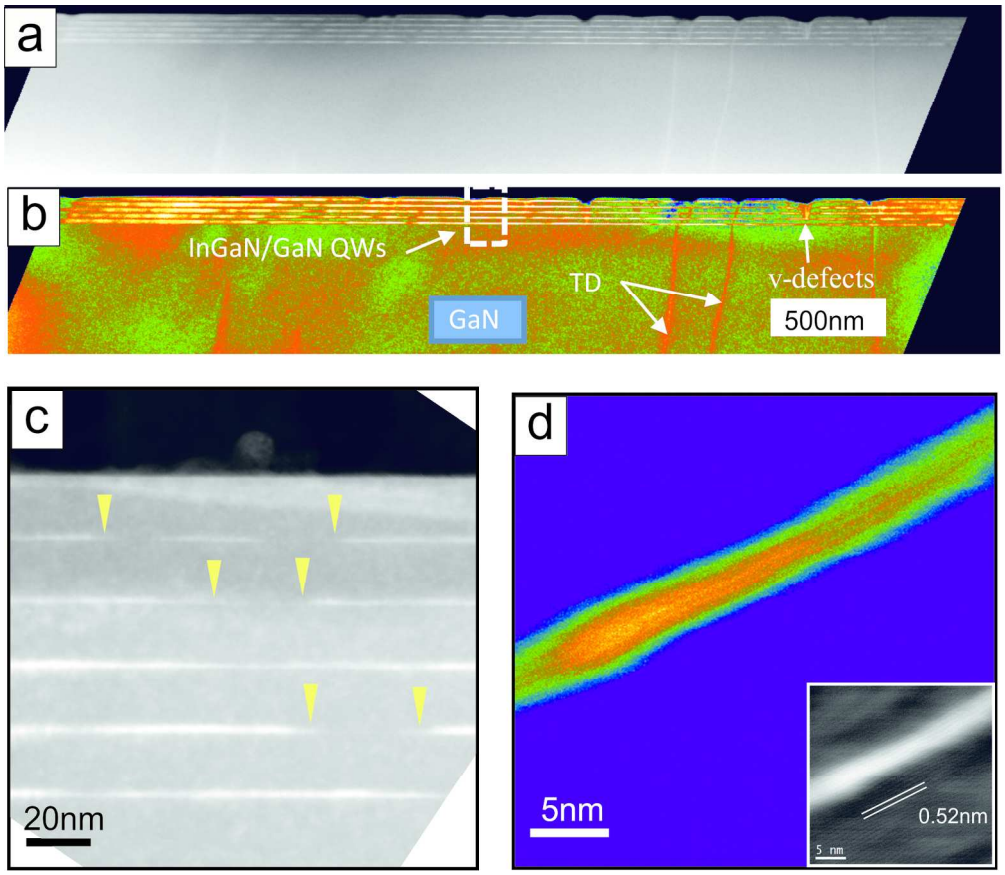

a-b) Low magnification HAADF-STEM micrograph of the QW sample and its temperature scale. c) Micrograph showing the discontinuities in the wells (marked with inverted yellow triangles). c) High magnification Z-contrast image of a QW in color scale where InN fluctuations can be noticed, the inset shows the original image in grey scale.
177x153mm (300 x 300 DPI)

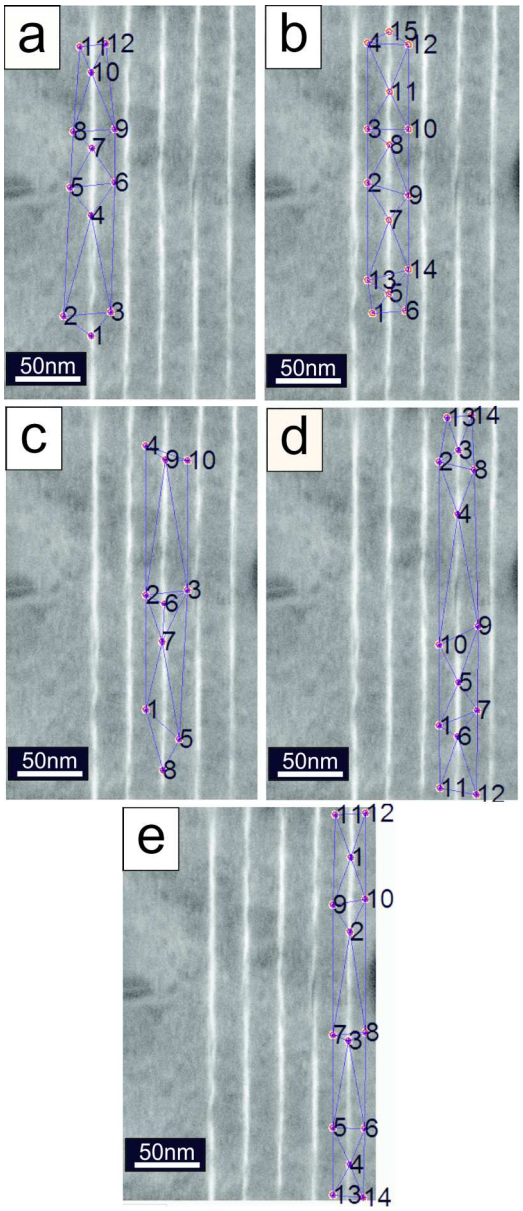

(a-e) HAADF-STEM images showing the meshed SRs of the QWs 1 to 5 respectively with their LCPs.
85x197mm (300 x 300 DPI)

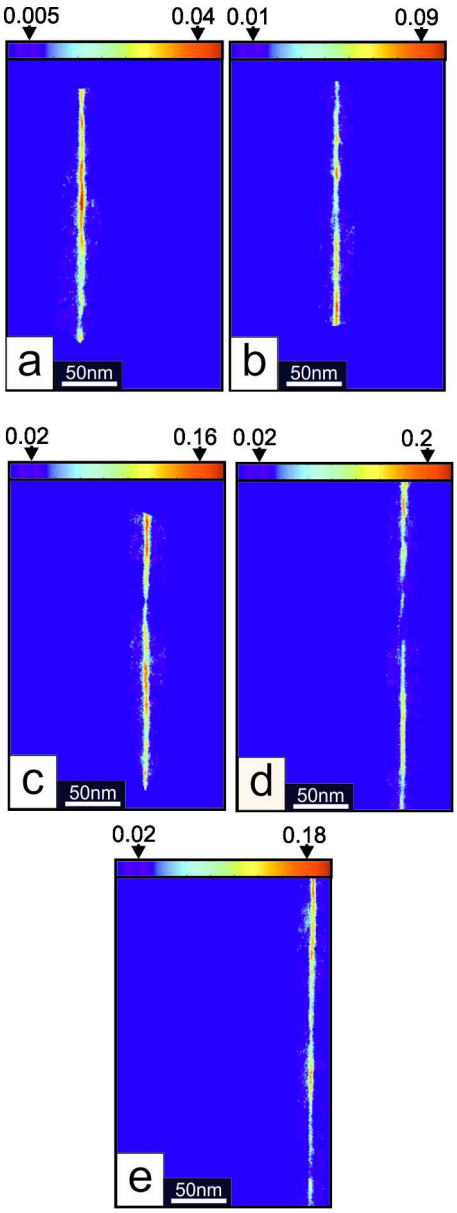

a-e) shows the composition maps of the QWs 1-5 respectively, before normalization.
85x227mm (300 x 300 DPI)

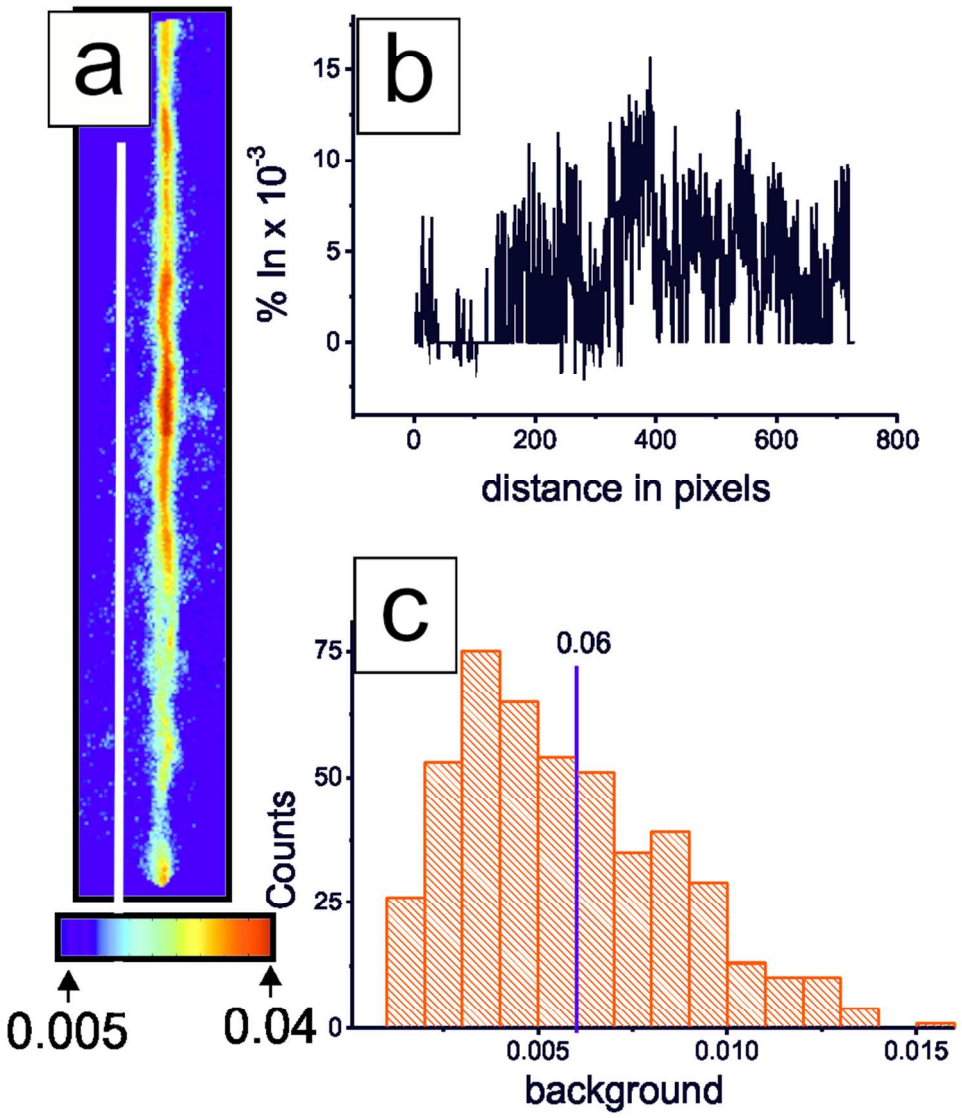

Figure 11. Composition map of the QW, the white line indicated the position from where the noise was measured. b) Shows the line profile c) the histogram of the background fluctuations.
84x98mm (300 x 300 DPI)

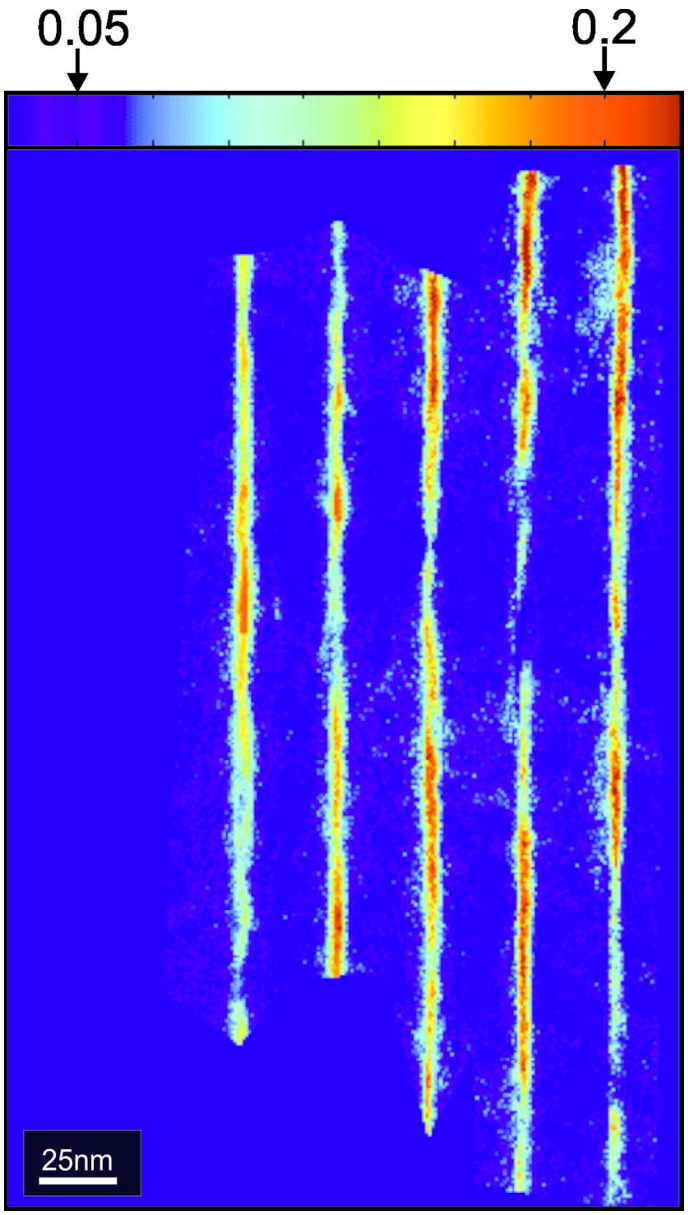

Temperature scale image color compositional map finally obtained for the InGaN region analyzed.
85x150mm (300 x 300 DPI)

QW / LCP	QW-1	QW-2	QW-3	QW-4	QW-5
1	1.61	0	0	0	9.6
2	0	0	0	0	8.52
3	0	0	0	13.45	8.14
4	2.82	0	0	9.45	5.95
5	0	7.17	0	7.51	0
6	0	0	7.19	6.52	0
7	3.06	5.73	6.42	0	0
8	0	1.69	5.41	0	0
9	0	0	11.7	0	0
10	0.89	0	0	0	0
11	0	3.4		0	0
12	0	0		0	0
13		0		0	0
14		0		0	0
15		2.42			
16		0			